ORIGINAL PAPER

High and selective adsorption of methylene blue using N-rich, microporous metal–organic framework [ZnBT(H$_2$O)$_2$]$_n$

Elham Asadi[1] · Mohammad Bakherad[1] · Mohammad Hadi Ghasemi[2]

Abstract

The first green application of N-rich metal–organic framework to selective adsorption of cationic dye (Methylene Blue) in the aqueous environment was investigated. In this paper, the [ZnBT(H$_2$O)$_2$]$_n$ synthesis method was optimized to increase yield and reduce energy consumption. The synthesis time was reduced to 1/3 (24 h), and the molar ratio of the compounds was changed to [metal salt (3): ligand (3): solvent (1)]. The high nitrogen MOF was characterized using X-ray diffraction, Brunauer–Emmett–Teller, scanning electron microscopy, energy-dispersive X-ray, thermogravimetric analysis/differential scanning calorimetry and Fourier-transform infrared spectroscopy. Also, the ability of selective adsorption towards cationic and anionic pollutants in aqueous solution was carefully investigated. Further studies revealed that the MOF was microporous ($r_p = 1.21$ nm) and demonstrated the ability to selectively and rapidly adsorption of methylene blue (MB) compared to the larger cationic dye (rhodamine B (RhB)) and the anionic dye (methyl orange (MO)) within 10 min. The removal percentage of MB, MO and RhB from the initial dye concentration (20 mg/L) was 98%, 4% and 2%, respectively. Interestingly, this MOF demonstrated an excellent adsorption capacity of MB (458 mg/g) compared to MO and RhB due to electrostatic interaction. Results of MB adsorption onto [ZnBT(H$_2$O)$_2$]$_n$ confirmed the pseudo-second-order kinetics ($R^2 = 0.999$) and the Langmuir isotherm ($R^2 = 0.861$).

Keywords Selectivity adsorption · N-rich MOF · Methylene blue · Isotherm · Kinetic

Introduction

Water resources have been reduced due to unplanned industrial growth. Therefore, water reclamation from diverse effluents is necessitated [1]. The contamination of colored effluent is a big concern and challenge due to the presence of toxic organic dyes [2]. The worldwide utilization of pigments and dyes in different industries, for example, cosmetics, textiles, plastic, food, pharmaceutical, paper, printing, rubber, and other industries has been widely documented and identified [3–5]. It is approximated more than 1×10^5 dyes are generated over 7×10^5 ton yearly. In the world,

more than ten thousand tons of toxic dyes are consumed in the textile industry annually and one percent of them are discharged into the wastewater [6]. Synthetic dyes have dangerous effects on living beings and the environment. Many dyes are poisonous, cause cancer, and death [7, 8]. The main problem is that these organic dyes have high chemical stability and low biodegradability in the aqueous solution and are present in large amounts in wastewater, which is very harmful to the environment [9]. Synthetic dyes don't exhibit molecular stability and are classified as anionic, nonionic, and cationic dyes because of their charge [10]. Methylene blue (MB) is often used as cationic dye and a major part of textile industrials wastewater [11]. Studies have shown that exposure to methylene blue can cause damage to skin and eye [12]. Direct use of MB causes indigestion, tissue necrosis, high heart rate, vomiting and nausea [13]. The mentioned concerns lead to the treatment of colored wastewaters using effective and efficient methods. Thus, the development of an advanced and effective treatment method for the removal of cationic dyes (MB) from wastewater is regarded as essential to maintain a healthy and safe

✉ Elham Asadi
asadi66elham@yahoo.com

✉ Mohammad Bakherad
m.bakherad@yahoo.com

1 Faculty of Chemistry, Shahrood University of Technology, 3619995161 Shahrood, Iran

2 Applied Chemistry Research Group, ACECR-Tehran University, Tehran, Iran

environment. Several processes have been reported on the effective removal of toxic and hazardous substances from aqueous solutions such as electrocoagulation [14], physical [15], chemical [15], photocatalytic degradation [16], biological methods [15], oxidation [17], and adsorption [18, 19].

Among all available methods for wastewater treatment, physical adsorption received considerable attention due to its simplicity of design, insensitivity to hazardous pollutants, inexpensive, the convenience of operation [20]. To date, lots of low cost and natural absorbents are reviewed such as clay [21], activated carbon [22, 23], rice husk [24], carbon nanotubes [25], fruit peel [26], sugarcane [27], membrane [28], metal–organic frameworks (MOFs) [29–38] and other porous materials.

Metal–organic frameworks (MOFs) have been considered as a new category of nanoporous material [39, 40]. Depending on the selection of the synthesis conditions, organic ligands, and metal nodes, self-assembled MOF structures can have a high variety of dimensions and topologies [41]

The most important interaction in forming MOFs is the covalent coordinating bond while other kinds of interactions such as π–π stacking, van der Waals forces, and hydrogen bonding also play a role in formation [42–45]. The properties including high tenability of pore size and shape, low density, high pore volume, wide surface area, greater adsorption sites, and unparalleled structural characteristics make them the materials of importance in the field of adsorption [46, 47]. They have been used for varied purposes such as gas storage [48], separation of gas [49], drug delivery [50], luminescence [51], heterogeneous catalysis [52], and pollutants adsorption [18, 53, 54]. MOFs based on the functional groups on the surface and the type of their ligands display various properties [55]. The framework charge (i.e., anionic, neutral, or cationic) of MOFs also has a large effect on their performance [56–58]. MOFs with high selectivity in the separation of pollutants and due to the high power in the separation of dye and chemical mixtures during the treatment of industrial effluent [59, 60], and also as a color detection sensor have attracted the attention of researchers [60].

In coordination chemistry, tetrazole-containing ligands have attracted much attention due to their large number coordination state, which can lead to the formation of a large combination with different dimensions and topology. Bis-tetrazoles and their derivatives have been considered by researchers owing to their potential anionic properties, high nitrogen content, and divers coordination modes [62–64]. Several studies have been focused on tetrazole-based MOFs to date, but only a few of them have investigated surface properties, the porosity, structural topology, and π–π stacking. These properties may influence in selective separation of dyes.

$[ZnBT(H_2O)_2]_n$ consist of 5,5′-bistetrazolate (BT^{2-}) which coordinates with Zn(II). This MOF is crystallized in the monoclinic space group and is a mononuclear molecule. The BT^{2-} ligand connects to three different Zn atoms to form one-dimensional chain structure. The one-dimensional chain structures of $[ZnBT(H_2O)_2]_n$ are closely connected by hydrogen bonds to form a three-dimensional supramolecular network, because Zn^{2+} is hexa-coordinated by four nitrogen atoms from three BT^{2-} and two oxygen atoms from water molecules. In this structure, one of the dianionic bistetrazole ligand acts as a chelating ligand [63].

The purifier production of anionic Zn-organic framework includes the use of safe solvents. A literature review illustrated that the $[ZnBT(H_2O)_2]_n$ metal–organic framework was not used for dye adsorption from water. Herein, we report the optimal method of $[ZnBT(H_2O)_2]_n$ synthesis to increase yield and reduce energy consumption and examine its green properties to remove toxic dye contaminants. The electron density due to the resonance of the tetrazole electrons in the ligand causes the $[ZnBT(H_2O)_2]_n$ anionic surface and this feature has been considered for the selective separation of cationic dyes. Anionic MOF; $[ZnBT(H_2O)_2]_n$ exhibits excellent adsorption capacity of methylene blue (MB) as compared with methyl orange (MO) and rhodamine B (RhB) due to electrostatic interaction and microporous structure. H_2BT and $[ZnBT(H_2O)_2]_n$ were characterized using $^{13}CNMR$, ^1HNMR, XRD, BET, SEM, EDX/mapping, TGA/DSC, and FTIR. The dye adsorption kinetics and isotherm data were investigated.

Experimental

Methylene blue, rhodamine B and methyl orange were used as the model pollutants. Sodium cyanide, sodium azide, manganese (IV) oxide, and $Zn(NO_3)_2.6H_2O$ were purchased from Merck. Other chemicals with analytical grade were used without purification. PerkinElmer Spectrum infrared spectrometer was used to record Fourier transform infrared (FTIR) spectra for studying the surface groups of ligand and adsorbents. ^1H and $^{13}CNMR$ spectra were recorded on a Bruker (Avance DRX-400) spectrometer at 400 and 100 MHz, respectively. The X-ray diffraction (XRD) patterns ware recorded with a PW1730 Philips X-ray diffractometer at room temperature. The morphological characteristics of the synthesized material were observed using scanning electron microscopy (SEM, Quantum 200) to estimate their probable composition. Distribution of elements was obtained using energy-dispersive X-ray (EDX) spectroscopy element mapping (Element silicon grift). Thermogravimetric analysis (TGA) coupled to differential scanning calorimetry (DSC) was carried out with a STA 1500 (Rheometric scientific) at a heating rate of 10 °C·min^{-1}. The BET was indicated by

BELSORP-mini II, and the contaminant concentration in wastewater was measured by UV–Visible spectrophotometer (Hitachi 3100).

Synthesis of 5,5′-bistetrazole (H$_2$BT)

5,5′-bistetrazole was prepared similar to the literature procedure [65]. To a solution of 1.0 mol of NaCN and 1.0 mol of NaN$_3$ in 500 mL of water were added 0.5 mol of MnO$_2$. Then, with vigorous stirring and cooling so as to maintain the temperature between 8–13 °C, a solution consisting of 1.0 mol of 96% H$_2$SO$_4$, 1.3 mol of glacial acetic acid, 0.004 mol CuSO$_4$ and 200 mL of water was added in solution. The temperature of the resultant slurry was then slowly raised over 1 h to 85 °C and held at this temperature for 2 h. The mixture was cooled to room temperature, the solution was filtered, and the salt was washed with water. The manganese salt suspended in 0.7 mol of Na$_2$CO$_3$ and the suspension was stirred for 1 h and the slightly green filtrate acidified with concentrated hydrochloric acid to pH 1. The precipitating white solid was filtered and dried. Also, concentration of the filtrate to half volume, yielded more product. Total yield: 46.7 g of Very bright yellow crystals. m.p. 259–260 °C; FTIR (KBr, cm^{-1}): $\nu = 3391$(m), 3016(s), 2807(vs), 2695(vs), 1678(w), 1529(m), 1378(s), 1282(s), 1225(w), 1105(vs), 1069(m), 1017(vs), 858(m), 617(m), ^{1}HNMR (d6-DMSO, 400 MHz, ppm): $\delta = 9.36$ (s, 1H, CN$_4$H); ^{13}CNMR (d6-DMSO, 100 MHz, ppm): $\delta = 148.2$ (s, CN$_4$).

Optimization Synthesis of [ZnBT(H$_2$O)$_2$]$_n$

The synthesis of the [ZnBT(H$_2$O)$_2$]$_n$ metal–organic framework was performed by changing the amount and ratio of materials as well as the optimized time (Scheme 1) and as follows [63]. In this work, the amount of materials has been multiplied compared to the values reported in the previous article and to increase the yield, the molar ratio of metal salt, ligand and solvent has been changed to (3: 3: 1) and also the hydrothermal synthesis time to 1/3 has decreased. In the first was dissolved 14.39 mmol H$_2$BT ligand in 60 mL of water solvent, then was added 2.88 mmol of Zn(NO$_3$)$_2$.6H$_2$O salt little by little to the reaction vessel. It was stirred on a magnetic stirrer for 20 min to conversion the colorless solution into a white mixture. The mixture was put into a 100-mL linear stainless-steel reactor. The reactor was heated to 160 °C for 24 h and then cooled to room temperature. The product yield is 0.593 g (white crystal). FTIR (KBr, cm^{-1}): 3370(w), 2341(m), 2233(m), 1623(m), 1450(s), 1363(m), 1333(m), 1236(m), 1207(m), 1179(m), 1109(m), 1073(m), 1026(m), 737(m), 618(m), 486(m), DSC (10 °C min^{-1}): Td, 337.8 °C.
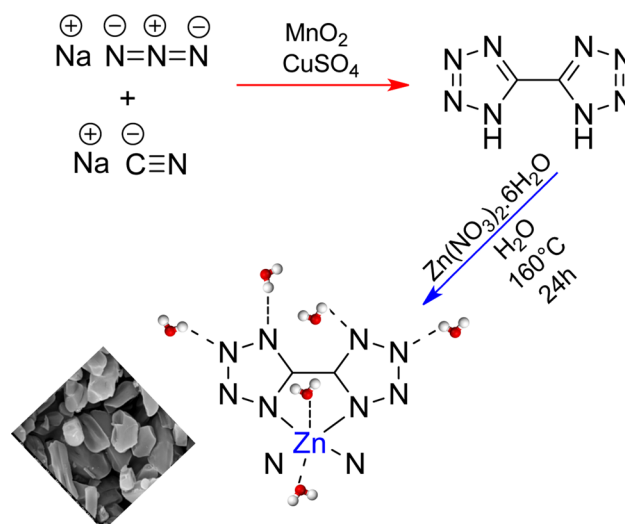
Scheme 1. Synthesis of H$_2$BT and [ZnBT(H$_2$O)$_2$]$_n$

Dye adsorption

The dye removal experiments were investigated by mixing various quantity of activated [ZnBT(H$_2$O)$_2$]$_n$ (0.003, 0.005, 0.007, 0.009 g) into dye molecules, methyl orange (MO), methylene blue (MB) and rhodamine B (RhB) in 100 mL of dye solution (20 mg/L) at natural pH. The MOF particles in solution samples were separated via centrifugation and then were measured by UV–Vis spectrophotometer at maximum wavelength of pollutants (MO: 465 nm, RhB: 554 nm and MB: 664 nm). Adsorption isotherms and kinetics were studied at various adsorbent dosages (MB: 20 mg/L and natural pH). All dye removal experiments were repeated three times and the average of A% was reported. The percentage relative standard deviation (RSD%) was about 3%.

Results and discussion

Characterization

H$_2$BT was prepared by [3 + 2] cycloaddition reaction between sodium azide and sodium cyanide; then by changing the cation between manganese and sodium, Na$_2$BT was made. Finally, by acidifying the test medium, H$_2$BT ligand was prepared [65]. Anionic MOF was made by coordination between Zn(II) and 5,5′-bistetrazole in optimized conditions by the hydrothermal method [63] and was used to selectively absorb the cationic dye (MB).

The surface morphology of the synthesized [ZnBT(H$_2$O)$_2$]$_n$ investigated with SEM (Fig. 1). The images illustrate that most of the morphology of [ZnBT(H$_2$O)$_2$]$_n$ crystals is in the form of a triangular prism and a small number of octahedron shapes.

Fig. 1 The SEM images of $[ZnBT(H_2O)_2]_n$

a)

b)

c)

d)

e)

f)
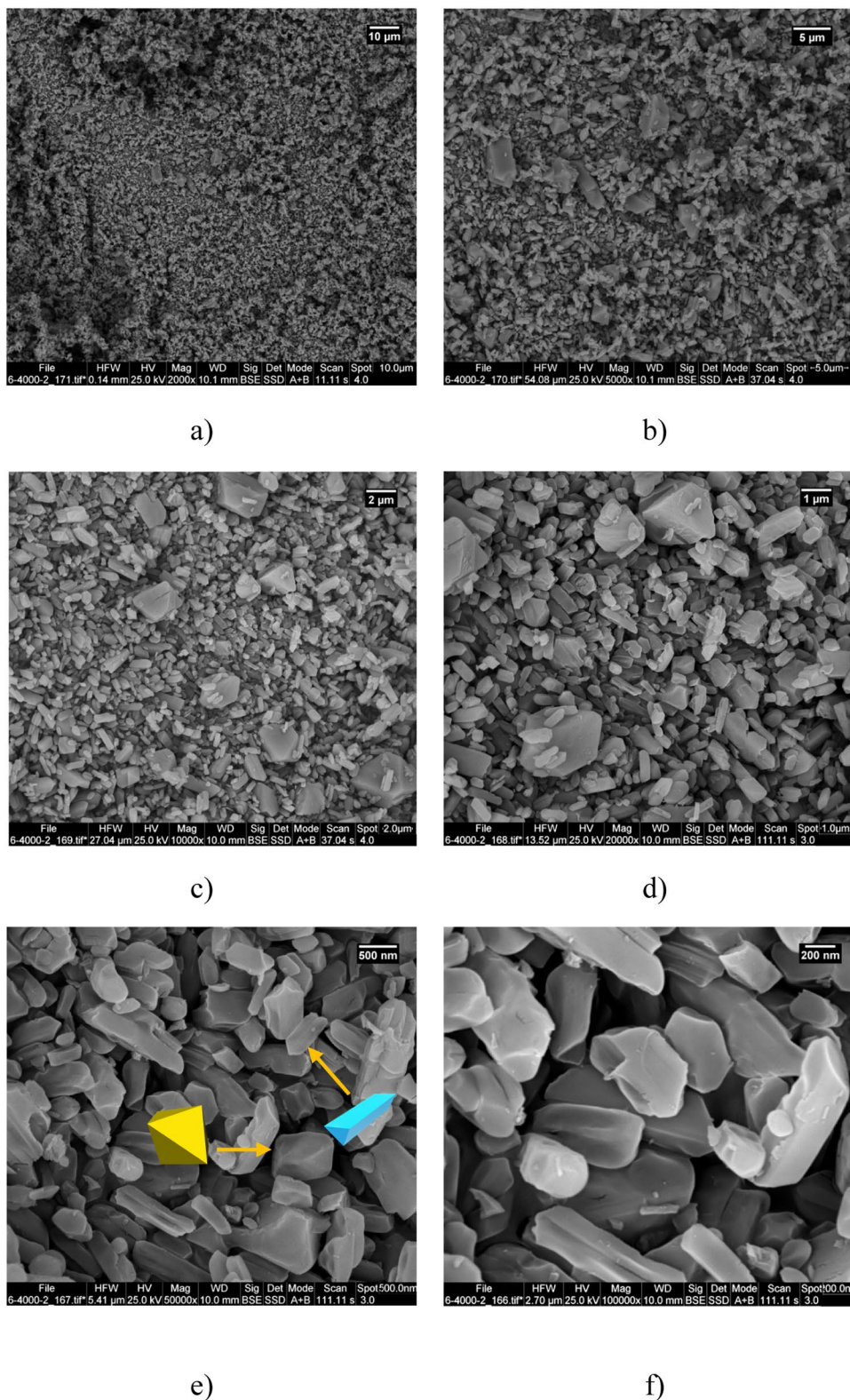
To further examine the distribution of Zn, N and C in $[ZnBT(H_2O)_2]_n$, energy-dispersive X-ray (EDX) spectroscopy element mapping using element silicon grift was carried out. The elemental maps of MOF, Zn, N, and C of $[ZnBT(H_2O)_2]_n$ showed in (Fig. 2a–d), respectively, and EDX spectrum in (Fig. 2f). The characteristic peaks of Zn, N, and C elements in EDX spectrum (Fig. 2.f) confirmed the coordination between Zn and 5,5′-bistetrazole at
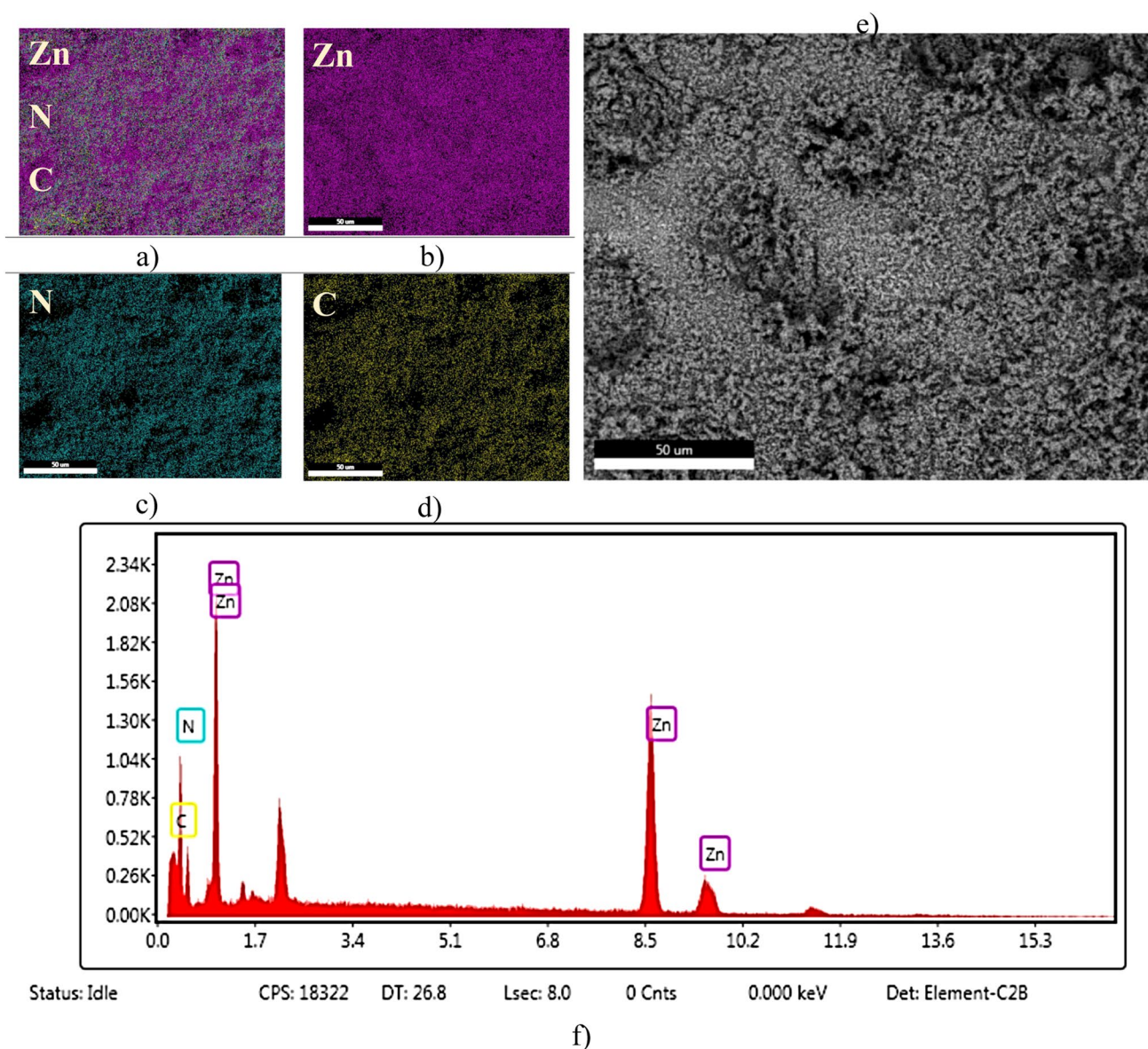
Fig. 2 Elemental maps of $[ZnBT(H_2O)_2]_n$, Zn, N and C (**a**), Zn (**b**), N (**c**), C (**d**), SEM image (**e**) and EDX spectrum (**f**) of $[ZnBT(H_2O)_2]_n$

the structure of anionic MOF. From the element mapping (Fig. 2a–d), it could clearly see that Zn, N, and C are uniformly dispersed in the whole $[ZnBT(H_2O)_2]_n$ particle.

FTIR spectroscopy is used for the identification of functional groups and structural elements in all materials. Characteristic vibrations of the aromatic 5,5′-bistetrazole and $[ZnBT(H_2O)_2]_n$ are shown in (Fig. 3). Due to the reaction between the 5,5′-bistetrazole ligand and Zn^{2+} in the FTIR spectrum, H–O–Zn stretching vibration at the range of 3370 cm^{-1} and H_2O-induced O–H bending vibration at 1623 cm^{-1} and also Zn–O stretching vibration at 737 cm^{-1} [66], appear which confirms the coordination of Zn^{2+} with oxygen in H_2O molecules. On the other hand, single N–H stretching vibration at the range of 3390 cm^{-1}, N–H bending vibration at the range of 1529 cm^{-1} [67], a group of stretching vibration due to the intermolecular hydrogen bonding of the N–H group in the 5,5′-bistetrazole at 3016–2400 cm^{-1} [67], and C=N stretching vibration at 1678 cm^{-1} disappear, and also the Zn–N stretching band at 486 cm^{-1} appears [68], which confirms coordination of ligand nitrogen with Zn^{2+} and formation of the $[ZnBT(H_2O)_2]_n$ structure. The presence of C–C, C–N and N–N vibrations at the range of 1363–1026 cm^{-1} in the FTIR spectrum of the anionic MOF and ligand (Fig. 3) confirms the presence of the H_2BT ligands in the MOF framework.
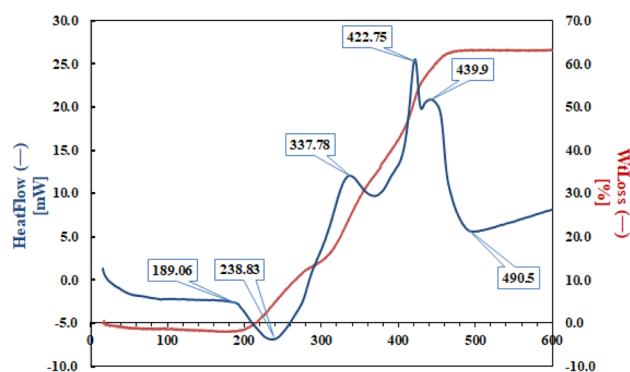
X-ray diffraction (XRD) was applied to illustrate the crystallinity of the synthesized MOF [63]. Figure 4a, b shows the simulated and synthetic pattern $[ZnBT(H_2O)_2]_n$
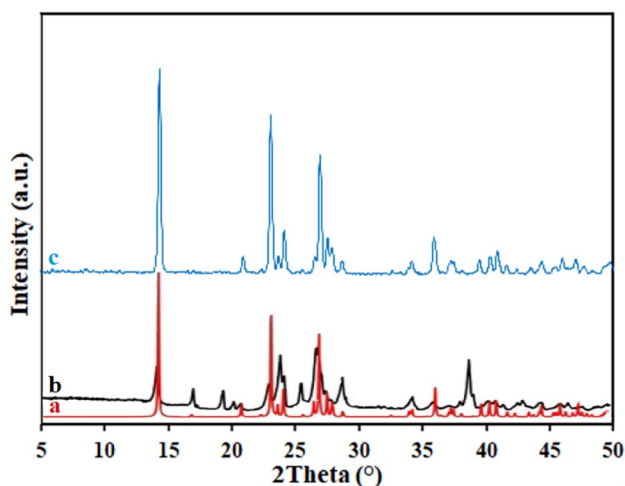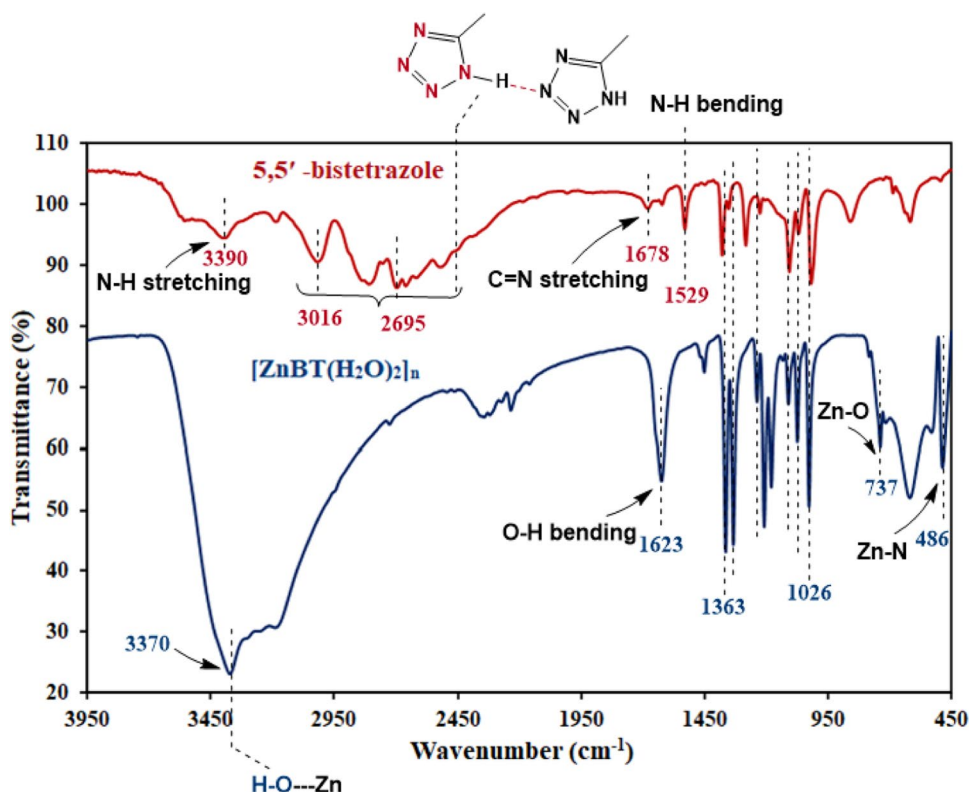
Fig. 4 The XRD pattern (**a** simulated, **b** $[ZnBT(H_2O)_2]_n$ from the literature [63]), **c** $[ZnBT(H_2O)_2]_n$

Fig. 5 TGA/DSC curve of $[ZnBT(H_2O)_2]_n$

derived from the previously published work, respectively. The peaks of anionic MOF are at (Fig. 4c) in excellent agreement with simulated pattern. When H_2BT and Zn^{2+} precursors were mixed, as a matter of fact, the anionic framework of $[ZnBT(H_2O)_2]_n$ makes a chance and is driving force for cation-exchange experiments. The cation is attracted to the electron cloud on 5,5′-bistetrazole. The XRD of the anionic MOF matches well with as-synthesized sample, confirming

the preservation of the crystalline framework with any impurity.

Figure 5 shows the TGA/DSC analysis of the anionic metal–organic framework; $[ZnBT(H_2O)_2]_n$. The thermal stabilities of synthetic MOF were investigated by using differential scanning calorimetry (DSC) and thermogravimetric analysis (TGA). The process of decomposition of the metal–organic framework is exothermic and endothermic. The results of TGA/DSC analysis show that from 189 to 490 °C, three weight losses occurred. Actually, 63.2% of the sample weight is related to bistetrazole ligand, moisture, residual solvent and 36.8% of the remaining weight is due

to ZnO. From 490 °C to a higher temperature, the weight of the sample remained constant. Due to moisture, residual solvent and phase change during the exothermic process, 13% of the sample weight was reduced in the temperature range of 189–290 °C. When water molecules are removed from the $[ZnBT(H_2O)_2]_n$ structure, the 3D structure becomes a 1D structure. During the exothermic process, 16% of the sample weight was decreased in the temperature range of 290–372 °C. As the temperature increases, the degradation of the structure is accompanied by the release of energy. The exothermic decomposition temperatures of $[ZnBT(H_2O)_2]_n$ were found at 337.78 °C as shown in Fig. 5. In the temperature range of 372–490 °C, 34% of the sample weight was reduced during the exothermic process. At this point, all the bistetrazole bonds are broken by the increased temperature, N_2 and CO_2 are released. Anionic MOF could be entirely decomposed at 500 °C. From 490 °C temperature to over, the process of weight loss has been constant, which indicated the presence of 36.8% zinc oxide. Due to the increase in temperature after the decomposition of the $[ZnBT(H_2O)_2]_n$ structure, zinc metal has reacted with oxygen, and zinc oxide has been obtained.

The MOF surface area, pore size, and porosity were determined using N_2 sorption. To confirm the adsorption property and its relationship with structural porosity, nitrogen gas adsorption, and desorption isotherms were done at 77 K with N_2 uptake of 0.1129 cm^3 g^{-1} at the relative pressure ($P/P_0 = 0.981$) which is too small and not considered. The surface area, average pore diameters, and total pore volume of $[ZnBT(H_2O)_2]_n$ were 25.189 cm^2 g^{-1}, 87.018 nm, and 0.1129 cm^3 g^{-1}, respectively. The total volume of the cavity is more than 0.6 ($P/P_0 = 0.981$), so the opening of the cavity is almost open, as summarized in the data indicated in Table 1. The results of the BJH analysis indicate, the abundance of the pore radius (r_p) was 1.2 nm, so the structure of $[ZnBT(H_2O)_2]_n$ is microporous.

Pollutant adsorption

The upward trend of industry development has attracted a lot of attention to the use of materials with high selectivity for wastewater treatment. Therefore, it is essential to study the selective adsorption ability for some absorbent in the removal of pollutants. To study the properties of electrostatic adsorption $[ZnBT(H_2O)_2]_n$ relative to organic dyes in the aqueous solution, two cationic dyes (MB, RhB) and an anionic dye (MO) were selected. The size of MB and MO is similar, but RhB is larger than them. The effect of time and adsorbent dosage on the removal of MB, MO, and RhB with a constant concentration (100 mL, 20 mg/L), pollutant adsorption by stirring-aided was performed for 12 min with various adsorbent dosages in the range of 0.003–0.009 g.
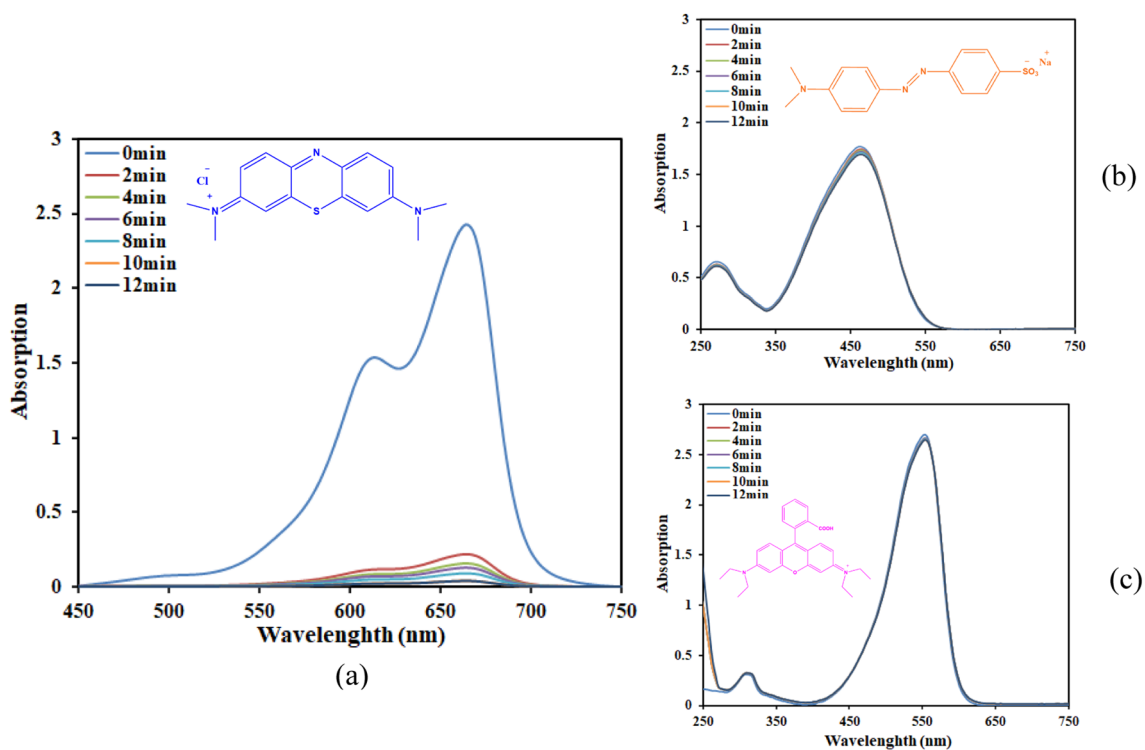
Comparison of dyes adsorption ability onto anionic [ZnBT(H₂O)₂]ₙ at various time and adsorbent dosage

The results of the UV–Visible spectrum show that increasing the amount of adsorbent only has an effect on increasing the adsorption of MB and has no effect on removing MO and RhB. Because the surface of $[ZnBT(H_2O)_2]_n$ is rich in nitrogen and electrons, so the methyl orange (anionic dye) is not absorbed due to electrostatic repulsion. On the other hand, the structure of the $[ZnBT(H_2O)_2]_n$ is microporous and it is not able to absorb the larger cationic dye (RhB). The results obtained from the UV–Visible spectrum in Fig. 6 indicate that methylene blue had excellent adsorption compared to MO and RhB.

Figure 7a shows the UV spectrum of the methylene blue removal in the presence of different dosage of the adsorbent. The methylene blue fades with increasing dosage of $[ZnBT(H_2O)_2]_n$ and the concentration of MB decreased to 1.61% of the initial concentration (20 mg/L). As the amount of adsorbent increases, the dye removal percentage increases, because the more electron-rich sites are made available for the adsorption of cationic molecules. In Fig. 7b, 0.003–0.009 g of activated $[ZnBT(H_2O)_2]_n$ was immersed into methylene blue solution (20 mg/L) at different times, separately. The results show that 90.89% of the initial concentration of MB was removed quickly within 2 min and after 10 min, the adsorption amount was reached 98.39%. Compared with the ability to adsorb MB with anionic MOF, only 4.14% of MO and 2.12% of RhB were removed in the presence of 0.009 g of $[ZnBT(H_2O)_2]_n$. The adsorption capacity of ZnBT is 458.24 mg/g which is much more than other absorbent MOFs (Fig. 7c) [69]. A comparative study of different MOFs with the present study for methylene blue removal is listed in Table 2.

Adsorption mechanism

$[ZnBT(H_2O)_2]_n$ demonstrated great removal efficiency for MB dye. The only a plausible mechanism of MB adsorption

Table 1 Surface properties of $[ZnBT(H_2O)_2]_n$

BET	
Surface area BET (S_{BET})	25.1892 (m^2 g^{-1})
Total pore volume (V_{total})	0.1129 (cm^3 g^{-1})
Average pore diameter	87.018 (nm)
BJH	
Pore volume (V_p)	0.1061 (cm^3 g^{-1})
Pore radius (r_p)	1.21 (nm)

Fig. 6 UV–Visible spectra of adsorption **a** MB, **b** MO, **c** RhB (20 mg/L) in aqueous solution onto [ZnBT(H$_2$O)$_2$]$_n$ (0.009 g) with different times (2–12 min)
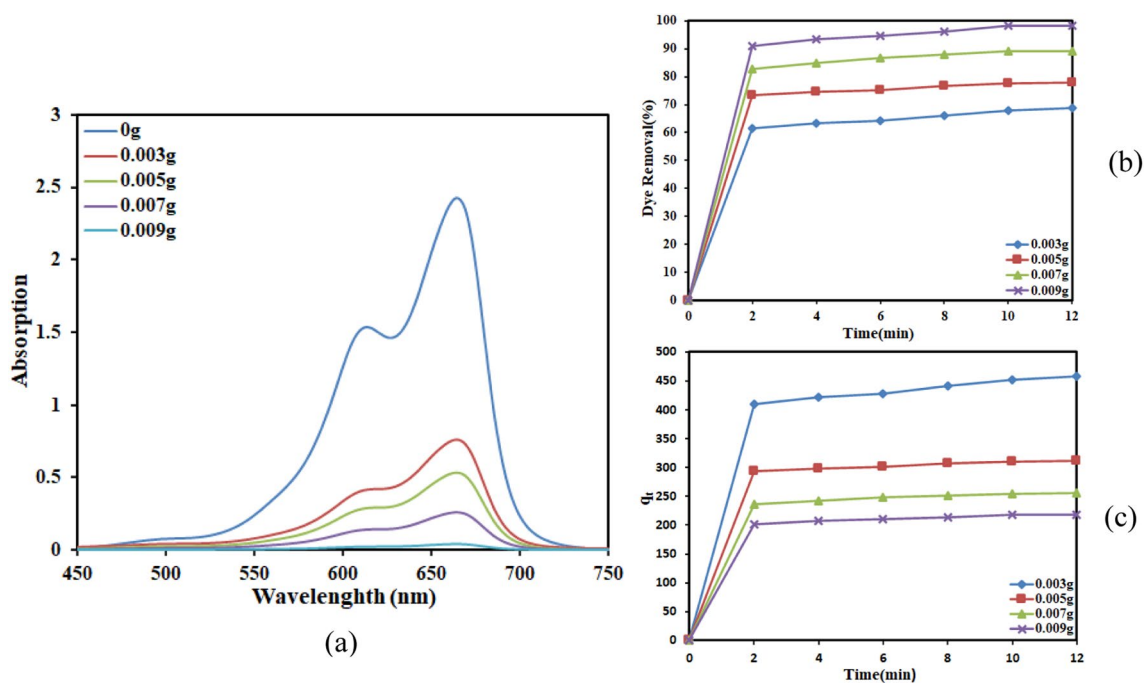
Fig. 7 **a** UV–Visible spectra, **b** dye removal%, **c** adsorption capacity of the adsorbate MB (20 mg/L) in aqueous solution onto [ZnBT(H$_2$O)$_2$]$_n$ with different times and dosages

on the $[ZnBT(H_2O)_2]_n$ surface is shown in Scheme 2. Synthesized MOF structure has high nitrogen content (47.16%), so there is a lot of electron density in the structure [63]. Electrostatic interaction occurred between methylene blue cation dye and electron-rich nitrogen structure. For this reason, the adsorption of MB is much higher than that of MO. The structure of $[ZnBT(H_2O)_2]_n$ is microporous and has very low porosity (Table 1), so the cationic dye rhodamine B was much less adsorbed than methylene blue due to its larger size.

Adsorption kinetics

To investigate the behavior of methylene blue on the $[ZnBT(H_2O)_2]_n$ surface, especially the adsorption mechanism and rate, kinetic models were used [18, 72, 73]. The linear equations of the pseudo-first-order (Eq. 1) and pseudo-second-order kinetics (Eq. 2) are expressed as follows.

$$\log\left(q_e - q_t\right) = \log\left(g_e\right) - k_1 t \tag{1}$$

$$t/q_t = 1/k_2 q_e^2 + t/q_e \tag{2}$$

The intraparticle diffusion model was used to evaluate the intraparticle diffusion resistance for the removal of methylene blue (Eq. 3).

$$q_t = k_p t^{1/2} + I \tag{3}$$

In order to measure the pseudo-first-order and pseudo-second-order constants and intraparticle diffusion, charts were plotted (Fig. 8). It was found that the correlation coefficient ($R^2 = 0.999$) second-order kinetics model is higher than the first-order model. The sorption of MB on $[ZnBT(H_2O)_2]_n$ surface matched well the pseudo-second-order model. The kinetic constants are shown in Table 3.
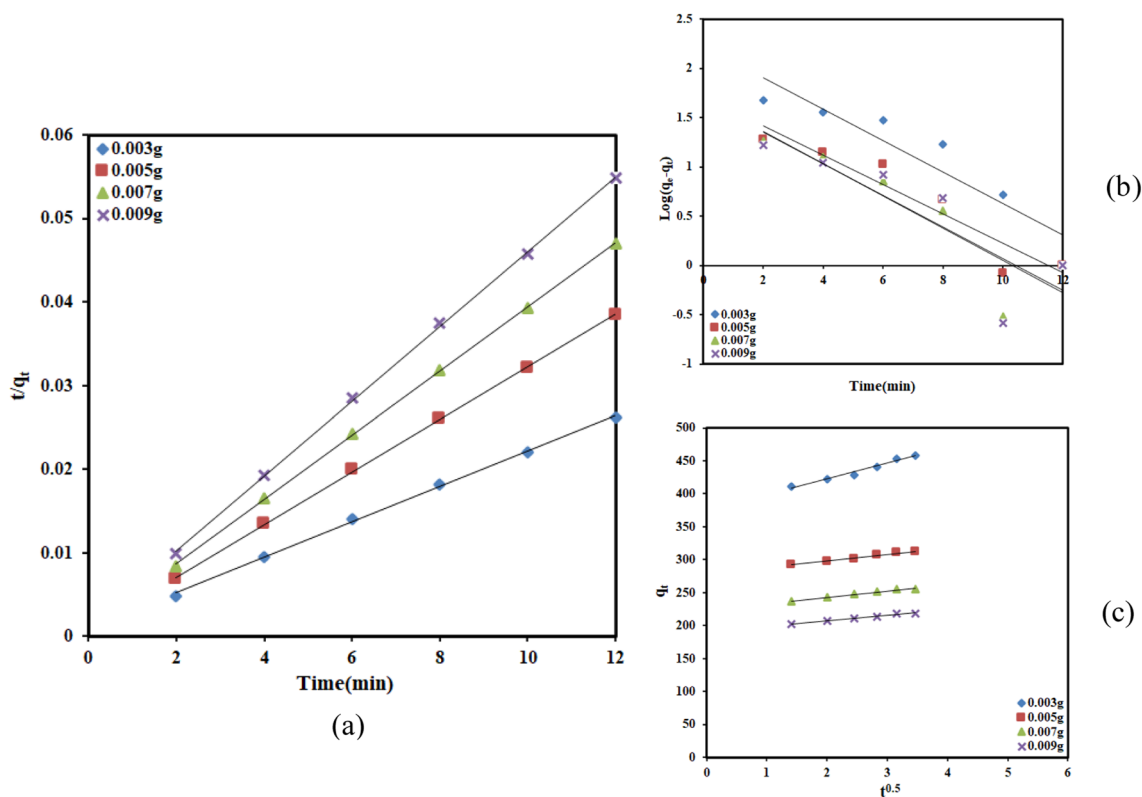
Adsorption isotherms

To investigate the process of MB adsorption on the anionic MOF and more accurately describe the adsorption mechanism, three isotherm models including the Langmuir, Freundlich, and Temkin isotherms were used to investigate the adsorption behavior in this work [18, 73]. The Langmuir adsorption model assumes that the adsorbent surface is monolayer in nature and that the adsorption process happens at homogeneous sites. As shown in Fig. 9, the isotherm was

Table 2 Methylene blue adsorption using different MOFs

Type of MOFs	Isotherm/kinetics	Adsorption capacity (mg/g)	References
Cu-BTC	Freundlich/pseudo-second order	96.4	[47]
UiO-66	Langmuir/pseudo-second order	107	[70]
$[(CH_3)_2NH_2]$ $[In(L)]\cdot 4H_2O\cdot 2DMF$	Langmuir/ pseudo-second order	281	[71]
HKUST-1	Langmuir/pseudo-second order	454	[70]
$[ZnBT(H_2O)_2]n$	Langmuir/pseudo-second order	458.24	This study
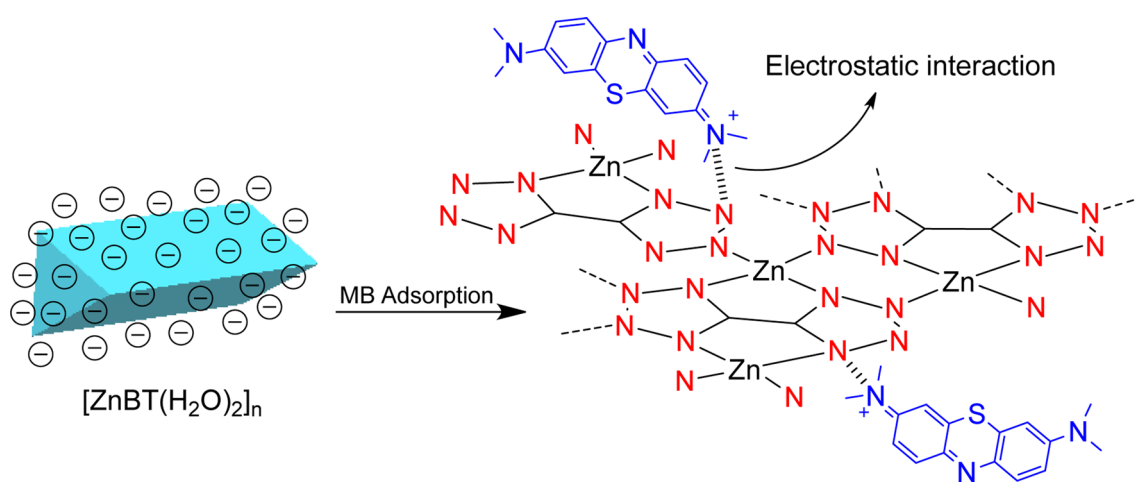
Scheme 2. Adsorption mechanism of the MB onto $[ZnBT(H_2O)_2]_n$

Fig. 8 **a** Pseudo-second order, **b** pseudo-first order of pollutant, **c** intraparticle diffusion of MB sorption by the synthesized $[ZnBT(H_2O)_2]_n$

plotted according to the Langmuir (Eq. 4) and the isotherm constants are shown in Table 4.

$$C_e/q_e = 1/K_L q_{max} + C_e/q_{max} \qquad (4)$$

The Freundlich isotherm is suitable for expressing the adsorption process at a heterogeneous surface related to a multilayer adsorption mechanism. In the Freundlich equation, the lower the value of the heterogeneity parameter ($1/n$), the higher the heterogeneity of the adsorbent

surface. Figure 9 is plotted based on the Freundlich isotherm equation (Eq. 5) and the constants extracted from the plot are given in Table 4.

$$\log q_e = \log K_F + 1/n \log C_e \qquad (5)$$

According to the Temkin isotherm, if the adsorption is chemical, the enthalpy of adsorption changes linearly with the adsorbent concentration. Figure 9 is plotted based on the Temkin equation (Eq. 6) and the Temkin isotherm constants are shown in Table 4.

Table 3 The kinetics and intraparticle diffusion constants of MB adsorption by $[ZnBT(H_2O)_2]_n$

Stirring		Pseudo-first order				Pseudo-second order			Intraparticle diffusion		
Absorbent	Dosage(g)	$Log(q_e-q_t)=Log(q_e)\cdot(K_1/2.303)t$				$(t/q_t)=(1/K_2 q_e^2)+(1/q_e)t$			$q_t=K_p t^{1/2}+I$		
		q_e(exp)	q_e(cal)	k_1	R^2	q_e(cal)	k_2	R^2	K_p	I	R^2
		(mg/g)	(mg/g)			(mg/g)			(mg/g min$^{1/2}$)	(mg/g)	
$[ZnBT(H_2O_2)]n$	0.003	458.2441	167.1091	0.3662	0.864	476.1905	0.0049	0.999	23.958	374.49	0.9788
	0.005	311.7707	51.8800	0.3408	0.895	312.5	0.0128	0.9998	9.904	278.3	0.9806
	0.007	311.7707132	48.7528	0.3754	0.8	263.1579	0.0144	0.9999	9.4438	223.99	0.9801
	0.009	218.6478523	46.6659	0.3685	0.737	222.2222	0.0156	0.9997	8.4519	190.22	0.9828
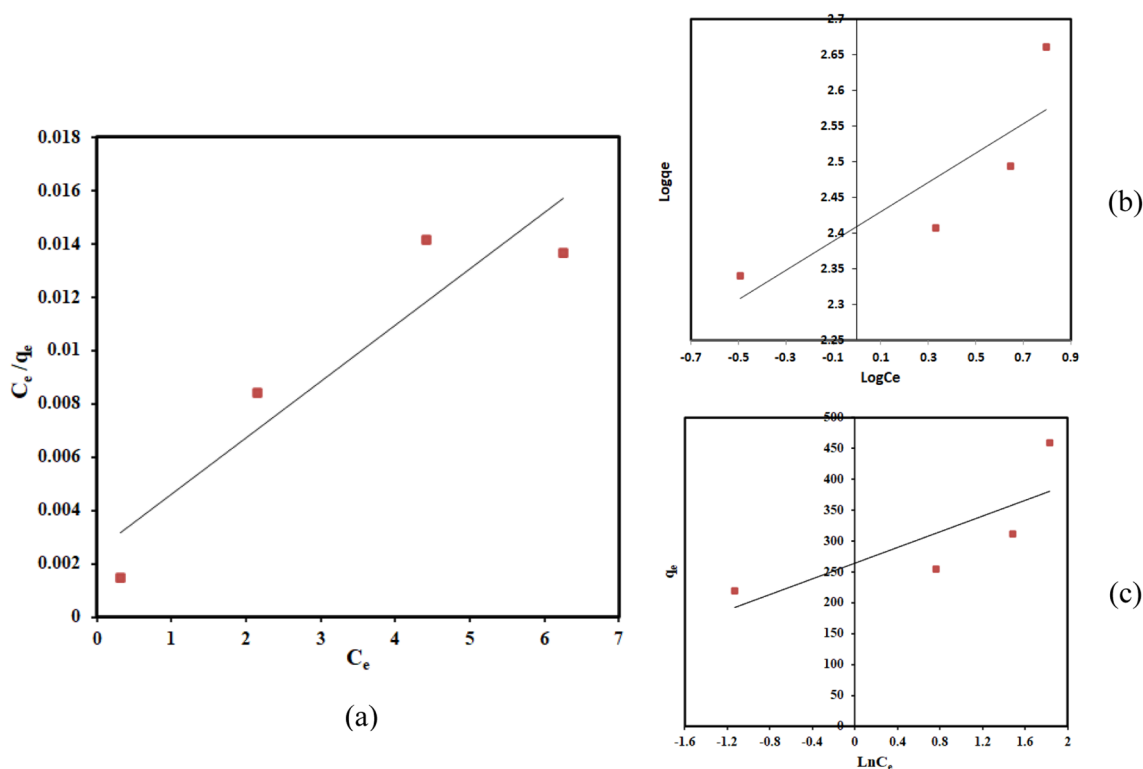
Fig. 9 The isotherm **a** Langmuir, **b** Freundlich, **c** Temkin of MB sorption by the synthesized anionic MOF

Table 4 The isotherm Langmuir, Freundlich and Temkin of MB adsorption by $[ZnBT(H_2O)_2]_n$

Isotherm	Equation	Plot	Parameters	Unit	$[ZnBT(H_2O)_2]_n$
Langmuir	$C_e/q_e = (1/K_L\,Q_{max}) + (1+Q_{max})C_e$	C_e/q_e VS. C_e	Q_{max}	mg/g	476.1905
			K_L	L/mg	0.84
	$R_L = 1/(1+K_L C_0)$		R^2	–	0.8611
			R_L	–	0.0562
Freundlich	$\mathrm{Log}\,q_e = \mathrm{Log}\,K_F + (1/n)\,\mathrm{Log}\,C_e$	$\mathrm{Log}\,q_e$ VS. $\log C_e$	$1/n$	–	0.2054
			K_F	L/mg	256.8029
			R^2	–	0.7226
Temkin	$q_e = B_T\,\mathrm{Ln}K_T + B_T\,\mathrm{Ln}C_e$	q_e VS. $\ln C_e$	B_T	–	63.352
			K_T	L/mg	64.8199
			R^2	–	0.633

$$q_e = B_T\,\ln K_T + B_T\,\ln C_e \qquad (6)$$

Based on the values of correlation coefficient (R^2) obtained from the Langmuir, Freundlich, and Temkin isotherms, R^2 values for the Langmuir model were better than that of the Freundlich and Temkin models (Table 4). Therefore, the adsorption of methylene blue on the $[ZnBT(H_2O)_2]_n$ followed the Langmuir isotherm. So, the adsorbent surface was monolayer and the adsorption process occurred on homogeneous sites.

Conclusion

In this work, the first green application of $[ZnBT(H_2O)_2]_n$ was investigated. N-rich MOF synthesis process was optimized by reducing the fabrication time (24 h) and changing the molar ratio of materials (3:3:1), to reduce energy consumption and increase efficiency. The $[ZnBT(H_2O)_2]_n$ were characterized using XRD, BET, SEM, EDX/mapping, TGA/DSC, and FTIR. The ability to selectively adsorption cationic and anionic contaminants onto MOF was investigated.

Methylene blue (MB), methyl orange (MO) and rhodamine B (RhB) removal at 20 mg/L of dyes were 98, 4, and 2% (RSD = 3%), respectively. In addition, $[ZnBT(H_2O)_2]_n$ showed a great adsorption capacity of MB (458 mg/g) compared to the larger cationic dye (RhB) and the anionic dye (MO) due to its microporous structure ($r_p = 1.21$ nm) and electrostatic attraction and repulsion. Kinetics and isotherm data of MB removal by anionic MOF obeyed pseudo-second-order kinetics ($R^2 = 0.999$) and the Langmuir isotherm ($R^2 = 0.861$).

References

1. D. Ghernaout, Open. Access. Libr. **7**, 1 (2020)
2. R.D. Saini, Int. J. Chem. Eng. Res. **9**, 121 (2017)
3. Y. Zhou, J. Lu, Y. Zhou, Y. Liu, Environ. Pollut. **252**, 352 (2019)
4. K. Piaskowski, R. Świderska-Dąbrowska, P.K. Zarzycki, J. AOAC Int. **101**, 1371 (2018)
5. M.A. Zazouli, F. Ghanbari, M. Yousefi, S. Madihi-Bidgoli, J. Environ. Chem. Eng. **5**, 2459 (2017)
6. G.D. Değermenci, N. Değermenci, V. Ayvaoğlu, E. Durmaz, D. Çakır, E. Akan, J. Clean. Prod. **225**, 1220 (2019)
7. M.A. Hassaan, A. El Nemr, Am. J. Environ. Sci. **1**, 64 (2017)
8. B. Kamarehie, A. Jafari, M. Ghaderpoori, M.M. Karami, K. Mousavi, A. Ghaderpoury, Data Brie. **20**, 903 (2018)
9. O. Leščinskis, R. Švinka, V. Švinka, Key Eng. Mater. **788**, 83 (2018)
10. S. Saber Samandari, H. Joneidi Yekta, M. Mohseni, Chem. Eng. J. **308**, 1133 (2017)
11. J. Fito, S. Abrham, K. Angassa, Int. J. Environ. Res. **14**, 501 (2020)
12. S. Sharma, A. Hasan, N. Kumar, L.M. Pandey, Sci. Pollut. Res. **25**, 21605 (2018)
13. T.C. Egbosiuba, A.S. Abdulkareem, A.S. Kovo, E.A. Afolabi, J.O. Tijani, M. Auta, W.D. Roos, Chem. Eng. Res. Des. **153**, 315 (2020)
14. D.T. Moussa, M.H. El-Naas, M. Nasser, M.J. Al-Marri, J. Environ. Manag. **186**, 24 (2017)
15. V. Katheresan, J. Kansedo, S.Y. Lau, J. Environ. Chem. Eng. **6**, 4676 (2018)
16. H. Anwer, A. Mahmood, J. Lee, K.H. Kim, J.W. Park, A.C. Yip, Nano Res. **12**, 955 (2019)
17. G. Boczkaj, A. Fernandes, Chem. Eng. J. **320**, 608 (2017)
18. N.M. Mahmoodi, M. Oveisi, E. Asadi, J. Clean. Prod. **211**, 198 (2019)
19. A. Alinejad, S. Sadeghi, M. Ghaderpoori, S. Sahebi, A. Ghaderpoury, A.A. Mohammadi, M.H. Saghi, Y. Gholampour, A. Khani Jeihooni, Int. J. Env. Anal. Chem. (2021). https://doi.org/10.1080/03067319.2019.1702170
20. M.N. Rashed, Organic Pollutants – Monitoring, Risk and Treatment (InTech, 2013), pp. 167–194
21. S. Bentahar, A. Dbik, M. El Khomri, N. El Messaoudi, A. Lacherai, Groundw. Sustain. Dev. **6**, 255 (2018)
22. N. Somsesta, V. Sricharoenchaikul, D. Aht-Ong, Mater. Chem. Phys. **240**, 122221 (2020)
23. B. Kamarehie, A. Jafari, M. Ghaderpoori, M.A. Karami, K. Mousavi, A. Ghaderpoury, Chem. Eng. Commun. **206**, 898 (2019)
24. Z. Shamsollahi, A. Partovinia, J. Environ. Manag. **246**, 314 (2019)
25. F. Mashkoor, A. N. Inamuddin, Environ. Chem. Lett. **18**, 605 (2020)
26. N.T.H. Nhung, B.T.P. Quynh, P.T.T. Thao, H.N. Bich, B.L. Giang, IOP Conf. Ser. Earth Environ. Sci. **159**, 1 (2018)
27. V. Yadav, J. Ali, M.C. Garg, J. Hazard. Toxic Radioact. Waste **25**, 04020067 (2020)
28. H. Koulivand, A. Shahbazi, V. Vatanpour, Chem. Eng. Res. Des. **145**, 64 (2019)
29. Z. Shi, C. Xu, H. Guan, L. Li, L. Fan, Y. Wang, R. Zhang, Colloids Surf. A Physicochem. Eng. Asp. **539**, 382 (2018)
30. H.M. Abd El Salam, T. Zaki, Inorgan. Chim. Acta. **471**, 203 (2018)
31. R.J. Yang Ying, C.X. Han, Q.T. Hu, H.M. Xu, J.H. Li, W. Zhang, Dalton. Trans. **47**, 3913 (2018)
32. K. Iman, M. Shahid, M.S. Khan, M. Ahmad, F. Sama, Cryst. Eng. Commun. **21**, 5299 (2019)
33. S. Yoon, J.J. Calvo, M.C. So, Curr. Comput.-Aided Drug Des. **9**, 17 (2019)
34. J.M. Yang, B.C. Yang, Y. Zhang, R.N.S.S. Yang Ji, Q. Wang, R.Z. Zhang, Microporous Mesoporous Mater. **292**, 109764 (2020)
35. N.M. Mahmoodi, M. Oveisi, A. Panahdar, B. Hayati, K. Nasiri, Mater. Chem. Phys. **243**, 122572 (2020)
36. T. Rasheed, A. A. Hassan, M. Bilal, T. Hussain, K. Rizwan, Chemosphere **259**, 127369 (2020)
37. M. Massoudinejad, M. Ghaderpoori, A. Shahsavani, M.M. Amini, J. Mol. Liq. **221**, 279 (2016)
38. A.A. Mohammadi, A. Alinejad, B. Kamarehie, S. Javan, A. Ghaderpoori, M. Ahmadpour, M. Ghaderpoori, Int. J. Env. Sci. Technol. **14**, 1959 (2017)
39. N.M. Mahmoodi, J. Abdi, Microchem. J. **144**, 436 (2019)
40. M. Massoudinejad, A. Shahsavani, B. Kamarehie, A. Jafari, M. Ghaderpoori, M.M. Amini, A. Ghaderpoury, Res. Rep. Fluo. **51**, 355 (2018)
41. J. Lyu, X. Zhang, K.I. Otake, X. Wang, P. Li, Z. Li, P. Bai, Chem. Sci. **10**, 1186 (2019)
42. R. J. Wei, H. G. Zhou, Z. Y. Zhang, G. H. Ning, D. Li, CCS Chem. **2**, 2045 (2020)
43. J. H. Deng, J. Luo, Y. L. Mao, S. Lai, Y. N. Gong, D. C. Zhong, T. B. Lu, Sci. Adv. **6**, 9976 (2020)
44. S. Zuluaga, P. Canepa, K. Tan, Y.J. Chabal, T. Thonhauser, J. Phys. Condens. Matter. **26**, 133002 (2014)
45. B. Wang, R.B. Lin, Z. Zhang, S. Xiang, B. Chen, J. Am. Chem. Soc. **142**, 14399 (2020)
46. S. Soni, P.K. Bajpai, C. Arora, Charact. Appl. Nanomat. (2019). https://doi.org/10.24294/can.v2i1.551
47. R. Kaur, A. Kaur, A. Umar, W.A. Anderson, S.K. Kansal, Mater. Res. Bull. **109**, 124 (2019)
48. N.A. Qasem, R. Ben-Mansour, M.A. Habib, Appl. Energy **210**, 317 (2018)
49. R.B. Lin, S. Xiang, H. Xing, W. Zhou, B. Chen, Coord. Chem. Rev. **378**, 87 (2019)
50. X. Shen, Y. Pan, Z. Sun, D. Liu, H. Xu, Q. Yu, J. Liu, Mini. Rev. Med. Chem. **19**, 1644 (2019)
51. T. Rasheed, F. Nabeel, Coord. Chem. Rev. **401**, 213065 (2019)
52. A. Dhakshinamoorthy, A. M. Asiri, H. García, Trends. Chem. **2**, 454 (2020)
53. C. Liu, L.Q. Yu, Y.T. Zhao, Y.K. Lv, Mikrochim. Acta. **185**, 342 (2018)
54. X. Song, P. Yang, D. Wu, P. Zhao, X. Zhao, L. Yang, Y. Zhou, Chem. Phys. **531**, 110655 (2020)
55. Z.J. Wang, L.J. Han, X.J. Gao, H.G. Zheng, Inorg. Chem. **57**, 5232 (2018)

56. G. Wu, J. Ma, S. Li, S. Wang, B. Jiang, S. Luo, L. Chen, Environ. Res. **186**, 109542 (2020)

57. D.K. Panda, K. Maity, A. Palukoshka, F. Ibrahim, S. Saha, ACS Sustain. Chem. Eng. **7**, 4619 (2019)

58. Y. Zhou, L. Qin, M.K. Wu, L. Han, Cryst. Growth. Des. **18**, 5738 (2018)

59. W. Gao, F. Liu, C.W. Pan, X.M. Zhang, J.P. Liu, Q.Y. Gao, Cryst. Eng. Commun. **21**, 1159 (2019)

60. X. Fang, B. Zong, S. Mao, Nanomicro. Lett. **10**, 1 (2018)

61. Q. Liu, B. Jin, Q. Zhang, Y. Shang, Z. Guo, B. Tan, R. Peng, Materials **9**, 681 (2016)

62. Y. Shang, B. Jin, R. Peng, Q. Liu, B. Tan, Z. Guo, Q. Zhang, Dalton Trans. **45**, 13881 (2016)

63. S. Chen, B. Zhang, L. Yang, L. Wang, T. Zhang, Dalton Trans. **45**, 16779 (2016)

64. Y. Feng, Y. Bi, W. Zhao, T. Zhang, J. Mater. Chem. A. **4**, 7596 (2016)

65. J.H. Nelson, N.E. Takach, R.A. Henry, D.W. Moore, W.M. Tolles, G.A. Gray, Magn. Reson. Chem. **24**, 984 (1986)

66. D. Huang, Q. Xin, Y. Ni, Y. Shuai, S. Wang, Y. Li, Y. Zhang, RSC Adv. **8**, 6099 (2018)

67. P. Hemalatha, M. Ganesh, M. M. Peng, W. S. Cha, M. Palanichamy, H. T. Jang, Springer, Berlin, Heidelberg. p. 445 (2012)

68. M. Bai, J.B. Zhang, L.H. Cao, Y.P. Li, D.Z. Wang, J. Chin. Chem. Soc. **58**, 69 (2011)

69. F.Y. Yi, J.P. Li, D. Wu, Z.M. Sun, Chem. Eur. J. **21**, 11475 (2015)

70. H. Liu, G. Gao, J. Liu, F. Bao, Y. Wei, H. Wang, Cryst. Eng. Commun. **21**, 2576 (2019)

71. M.R. Azhar, H.R. Abid, H. Sun, V. Periasamy, M.O. Tadé, S. Wang, J. Colloid Interface Sci. **490**, 685 (2017)

72. M. Massoudinejad, M. Ghaderpoori, A. Shahsavani, A. Jafari, B. Kamarehie, A. Ghaderpoury, M.M. Amini, J. Mol. Liq. **255**, 263 (2018)

73. A. Ghosh, G. Das, Microporous Mesoporous Mater. **297**, 110039 (2020)